

A simple Bessel module with tunable focal depth and constant resolution for commercial two-photon microscope

Ting Mo^{*,¶}, Yiran Liu^{†,¶}, Fatao Bie*, Zimin Dai*, Jin Chang*,
Hui Gong^{*,†,‡} and Wei Zhou^{*,†,‡,§}

*Britton Chance Center and

MoE Key Laboratory for Biomedical Photonics

Wuhan National Laboratory for Optoelectronics

Huazhong University of Science and Technology

Wuhan, P. R. China

†MoE Key Laboratory for Biomedical Photonics
Collaborative Innovation Center for Biomedical Engineering

School of Engineering Sciences

Huazhong University of Science and Technology

Wuhan, Hubei 430074, P. R. China

‡Research Unit of Multimodal Cross Scale
Neural Signal Detection and Imaging

Chinese Academy of Medical Sciences

HUST-Suzhou Institute for Brainsmatics

JITRI Suzhou, P. R. China

wzhou@mail.hust.edu.cn

Received 24 March 2023

Revised 25 May 2023

Accepted 25 May 2023

Published 30 June 2023

The volumetric imaging of two-photon microscopy expands the focal depth and improves the throughput, which has unparalleled superiority for three-dimension samples, especially in neuroscience. However, emerging in volumetric imaging is still largely customized, which limits the integration with commercial two-photon systems. Here, we analyzed the key parameters that modulate the focal depth and lateral resolution of polarized annular imaging and proposed a volumetric imaging module that can be directly integrated into commercial two-photon systems using conventional optical elements. This design incorporates the beam diameter adjustment settings of commercial two-photon systems, allowing flexibility to adjust the depth of focus while maintaining the same lateral resolution. Further, the depth range and lateral resolution of the

[§]Corresponding author.

[¶]These authors contributed equally to this work.

design were verified, and the imaging throughput was demonstrated by an increase in the number of imaging neurons in the awake mouse cerebral cortex.

Keywords: Volumetric imaging; Bessel beam; two-photon microscopy.

1. Introduction

Two-photon microscopy (2PM) has been considered as a promising technology for cell biology and neuroscience research which utilizes long wavelength light capable of penetrating deeper into the biological tissue.^{1–4} The process of 2PM requires high-energy density to excite two low-energy photons to emit a higher-energy photon making it a powerful tool to achieve excellent spatial resolution.^{5,6} Using 2PM, the excitation thickness of fluorescence molecule is around a few microns.⁷ Biological samples, however, are mostly three-dimensional (3D) structures, such as neurons and their networks, which present new challenges for 2PM imaging. Traditionally, Z-motor or piezo scans have been used to obtain 3D information.⁸ Although a point-by-point scan is generally considered to be useful because it guarantees a uniform resolution for the entire sample, it costs tens of seconds for volume data, leading to restrictions in capturing the dynamic activity of neurons.⁹ As this limitation is growing ever more important in the field of neuroscience, this demand has facilitated the design and development of rapid volumetric imaging.

Volumetric imaging can simultaneously probe images of different depths in a 3D tissue without axial scanning, which is usually achieved by multi-focus or extended depth of focus (DOF).¹⁰ The principle of DOF is to expand a point focus into a needle focus in the axial direction, increasing the area of the illumination. In volumetric imaging, the Bessel beam is a kind of nondiffraction beam, which has the property of self-recovery and long-distance transmission when propagating in biological tissues, resulting in elongated DOF.^{11–14} The Bessel beam can be transformed from a traditional Gaussian beam with spatial light modulator (SLM) or axicon, converting point illumination entirely to line illumination.¹⁵ This method provides an approach to monitoring tissue activity in a 3D network, which has successfully imaged calcium dynamics of zebrafish spinal projection neurons, human gastric cancer, and blood vessels of the mouse brain.^{16–19} However, extending DOF axially causes signals at different depths superimpose during detection because the Bessel beam outputs the projection of the volumetric data in the Z direction.

To avoid overlap, the labeled density of the fluorescence signal or DOF requires adjustments.

In this theory, based on scalar diffraction, the DOF is positively correlated with thickness and inversely correlated with the diameter of the annular distribution generated by the Bessel beam.^{20,21} However, Richards and Wolf showed that the vector properties of 2PM cannot be ignored to correctly describe the high numerical aperture (NA) focused beams in the nonparaxial regions.²² Moreover, 2PM is equipped with a high-NA objective and polarization state. Therefore, the description of the Bessel beam requires more comprehensive theoretical derivation.

For the generation of the Bessel beam, the SLM can form a series of DOF ranging from $15\text{ }\mu\text{m}$ to $400\text{ }\mu\text{m}$ through different concentric binary phase patterns on the computer.²³ However, the special components and bulky equipment make it difficult to merge with the commercial 2PM. On the other hand, an axicon-based system has the advantage of compactness and integrability but usually generates only one fixed DOF.^{24–28} Even if the DOF can be adjusted by moving the lens position, the method still requires a customized optical path,²⁹ which hampers its application in arbitrary 2PM. It is therefore important to perfect the theory of annular imaging under vector nature and establish a method that can be easily integrated into the existing 2PM.

In this work, we refined the theory based on vector diffraction analysis, confirming that the DOF is variable while maintaining stable lateral resolution on a high-NA system. Then, we verified it with fluorescent beads by measuring DOF and lateral resolution. Next, we observed the morphology of GFP-labeled neurons *in vivo* and recorded the calcium activity of GCaMP-labeled neurons under the visual stimulation of motion grating, focusing on comparing the changes in cell number regulated by different DOFs.

2. Materials and Methods

2.1. Tunable optical path of two-photon microscope

A Ti-sapphire laser (wavelength: 920 nm, repetition frequency: 80 MHz, output power: 1.35 W, pulse

width: 100 fs; Mai Tai HP, Spectra-Physics) and a commercial two-photon microscope system (FVMPE-RS, Olympus, Japan) were used to design the tunable optical path, equipped with a built-in module which can adjust the diameter of Gaussian beam. Before entering the scanner, a quarter wave plate (QWP) and a polarization beam splitter (PBS) were added to the optical path to flexibly switch between the original Gaussian beam mode which was circularly polarized, and Bessel beam mode which was linearly polarized. In the Bessel module, the incident Gaussian beam was converted into Bessel light through an axicon (AX252-B, Thorlabs) and a lens (AC254-050-B-ML, Thorlabs) was used to shape the light into a ring at its back focal plane. Besides, a pair of lenses (AC508-500-B-ML) were used to relay the Bessel ring onto the resonance scanning module of the commercial two-photon system. An objective with a high-NA (XLPlan N 25X, NA = 1.05, Olympus) was used to focus the annular ring beam into our sample. In volume imaging, for transverse scanning, two beams had the same mode. For axial scanning, the Gaussian beam required a step-moving sample platform, which was not necessary for the Bessel beam.

2.2. Preparation of bead samples

To measure the transverse and axial resolution, fluorescent beads ($0.2\text{ }\mu\text{m}$, 505/515, Thermo Fisher Scientific) were diluted with anhydrous ethanol at a ratio of 1:10,000 and prepared on slides. The samples were placed in the dark for 0.5 h to allow the alcohol to evaporate. The fluorescent beads were fixed to the slide, so the water droplets were imaged directly on the slide as immersion media.

2.3. Animals and preparation of *in vivo* experiment

Male C57/B6J mice were obtained from Beijing Vital River Laboratory Animal Technology Co., Ltd. Mice were maintained under conditions of $22 \pm 1^\circ\text{C}$ and $55 \pm 5\%$ humidity. All animal experiments were conducted by the Guidelines of the Animal Care Facility of Huazhong University of Science and Technology (HUST) and the experimental procedures on mice were approved by the Animal Ethics Committee of HUST.

The mice used for *in vivo* imaging were labeled with the GFP virus and rAAV-hSyn-GCaMP6s

virus, respectively. Cranial window surgery was performed on 2-month-old mice and imaging experiments were performed after 14 days of observation. Imaging experiments were performed on awake mice with their heads fixed under an objective lens. The stack was first scanned layer by layer with a Gaussian beam at a frame rate of 15 Hz. Then, the Gaussian beam and the Bessel beam were each used to conduct *in vivo* imaging. For GCaMP6s-labeled mice, the spontaneous responses of neurons were recorded within 3 s with external visual stimulation. The visual stimulation was motion grating in four directions.

2.4. Visual stimulation, image processing and data analysis

All image processing, visualization and analysis were carried out in ImageJ and MATLAB. For mouse *in vivo* imaging, the neurons at a depth of $0\text{--}100\text{ }\mu\text{m}$ under the Gaussian beam were subjected to Z projection and the Auto operation on brightness/contrast was adopted for both Gaussian beam and Bessel beam monolayer data to improve the visibility of neurons. The average intensity of the stack was also projected over multiple frames to improve the signal-to-noise ratio. When comparing the lateral resolution of the neurons, the intensity of the hand animation ROI was displayed for the neurons of interest. Statistical analysis and data regression were performed in GraphPad Prism.

The orientation selectivity index was used to quantify the strength of orientation preference as $\text{OSI} = (R_{\text{pref}} - R_{\text{ortho}})/(R_{\text{pref}} + R_{\text{ortho}})$.

3. Results

3.1. A ring principle with adjustable DOF and constant lateral resolution

The Bessel beam forms an annular distribution on the back focal plane of the objective lens, which is closely related to the imaging features. Considering the effects of linear polarization and high NA, we theoretically deduced how parameters such as ring width and ring radius would affect the DOF and lateral resolution based on vector diffraction theory. By referring to the analysis of Harold Dehez *et al.*,³⁰ we can obtain the approximation expressions of the

electric field of annular illumination:

$$\left\{ \begin{array}{l} E_X(r, z, \psi) = -iA[I_0(r, z) + I_2(r, z) \cos(2\psi)], \\ E_Y(r, z, \psi) = -iAI_2(r, z) \sin(2\psi), \\ E_Z(r, z, \psi) = -2AI_1(r, z) \cos\psi. \\ I_0(r, z) = I_0 J_0(kr \sin \alpha_0) \cdot \exp\left(-\frac{z^2}{z_0^2} - jkz \cos \alpha_0\right), \\ I_1(r, z) = I_0 J_1(kr \sin \alpha_0) \frac{\sin \alpha_0}{1 + \cos \alpha_0} \\ \quad \cdot \exp\left(-\frac{z^2}{z_0^2} - jkz \cos \alpha_0\right), \\ I_2(r, z) = I_0 J_2(kr \sin \alpha_0) \frac{1 - \cos \alpha_0}{1 + \cos \alpha_0} \\ \quad \cdot \exp\left(-\frac{z^2}{z_0^2} - jkz \cos \alpha_0\right), \end{array} \right. \quad (1)$$

where r , z and ψ are the cylindrical coordinates, and k is the wave vector. I_0 and z_0 are constants that depend on the angles α_0 and $\Delta\alpha$, corresponding to the ring radius R and the ring width ΔR in Fig. 1(a), respectively. According to the Richards-Wolf vector field equation for linear polarization,³¹ the intensity distribution can be described as follows:

$$\begin{aligned} I(r, \psi, z) &= |I_0(r, z) + I_2(r, z) \cos(2\psi)|^2 \\ &\quad + 4|I_1(r, z)|^2 \cos^2\psi + |I_2(r, z)|^2 \sin^2(2\psi), \end{aligned} \quad (2)$$

where ψ is the observation angle. Substituting Eq. (2) into Eq. (1), the intensity distribution at the focal point can be calculated as follows:

$$\begin{aligned} I(r, \psi, z) &= \frac{I_0^2}{(1 + \cos \alpha_0)^2} \exp\left(-\frac{2z^2}{z_0^2}\right) \\ &\quad \times [(1 + \cos \alpha_0)^2 J_0^2(kr \sin \alpha_0) \\ &\quad + 4\cos^2\psi \sin^2\alpha_0 J_1^2(kr \sin \alpha_0) \\ &\quad + (1 - \cos \alpha_0)^2 J_2^2(kr \sin \alpha_0) + 2\cos(2\psi) \\ &\quad \times (1 - \cos \alpha_0)(1 + \cos \alpha_0) J_0(kr \sin \alpha_0) \\ &\quad \times J_2(kr \sin \alpha_0)]. \end{aligned} \quad (3)$$

Using Eq. (3), we can estimate the DOF along z by $\frac{I(0,z)}{I(0,0)} = \frac{1}{2}$, and solve the transcendental equation of transverse resolution r by $\frac{I(r,z)}{I(0,z)} = \frac{1}{2}$:

$$z \approx Cz_0 \sqrt{2 \ln 2} = \frac{\lambda \sqrt{2 \ln 2}}{\pi \sin \alpha_0 \Delta\alpha}, \quad (4)$$

$$\begin{aligned} &J_0^2(kr \sin \alpha_0) + 4\cos^2\psi \frac{\sin^2 \alpha_0}{(1 + \cos \alpha_0)^2} J_1^2(kr \sin \alpha_0) \\ &\quad + \frac{(1 - \cos \alpha_0)^2}{(1 + \cos \alpha_0)^2} J_2^2(kr \sin \alpha_0) \\ &\quad + 2\cos(2\psi) \frac{(1 - \cos \alpha_0)}{(1 + \cos \alpha_0)} J_0(kr \sin \alpha_0) \\ &\quad \times J_2(kr \sin \alpha_0) = \frac{1}{2}. \end{aligned} \quad (5)$$

It can be seen from Eq. (4) that DOF is proportional to the wavelength λ , and is inversely proportional to the radius angle α_0 and the width angle $\Delta\alpha$. That means the DOF can be tuned by the radius R or the width ΔR in the annular ring. Another point worth noting is that Eq. (4) is consistent with Eq. (15) in Ref. 30.³⁰ This is because the expression of axial DOF does not include the observation angle ψ , therefore the formula is consistent under different polarizations. From Eq. (5), one can see that the lateral resolution r is only related to the radius angle α_0 in the case of a fixed wavelength λ and observation angle ψ , indicating that the lateral resolution r is only regulated by the ring radius R . Combining Eqs. (4) and (5), Fig. 1(b) describes the correlation between different ring parameters and the DOF and the lateral resolution. The result showed that the DOF decreases along with an increase in the ring width, while the lateral resolution remains unchanged regardless of the radius. Therefore, in the case of under linear polarization and high-NA, we theoretically can achieve adjustable DOF and constant lateral resolution by adjusting the ring width ΔR while keeping the ring radius R unchanged.

3.2. Tunable extended Bessel system

To achieve a ring-shaped field pattern, we simulated an axicon-based optical path model into commercial 2PM to convert Gaussian mode into a Bessel beam, which is a thin annulus light in the far field (Fig. 1(c)). In the back focal plane of the objective lens, the ring beam is focused, which is the initiator of axial extension of the depth of focus. We simulated the correlation between module parameters and the ring at the back focal plane of the objective by referring to the open Matlab code from the Na Ji group based on the vector diffraction theory.²⁹ Then, we found that changing the Gaussian diameter of the incident light before the axicon could

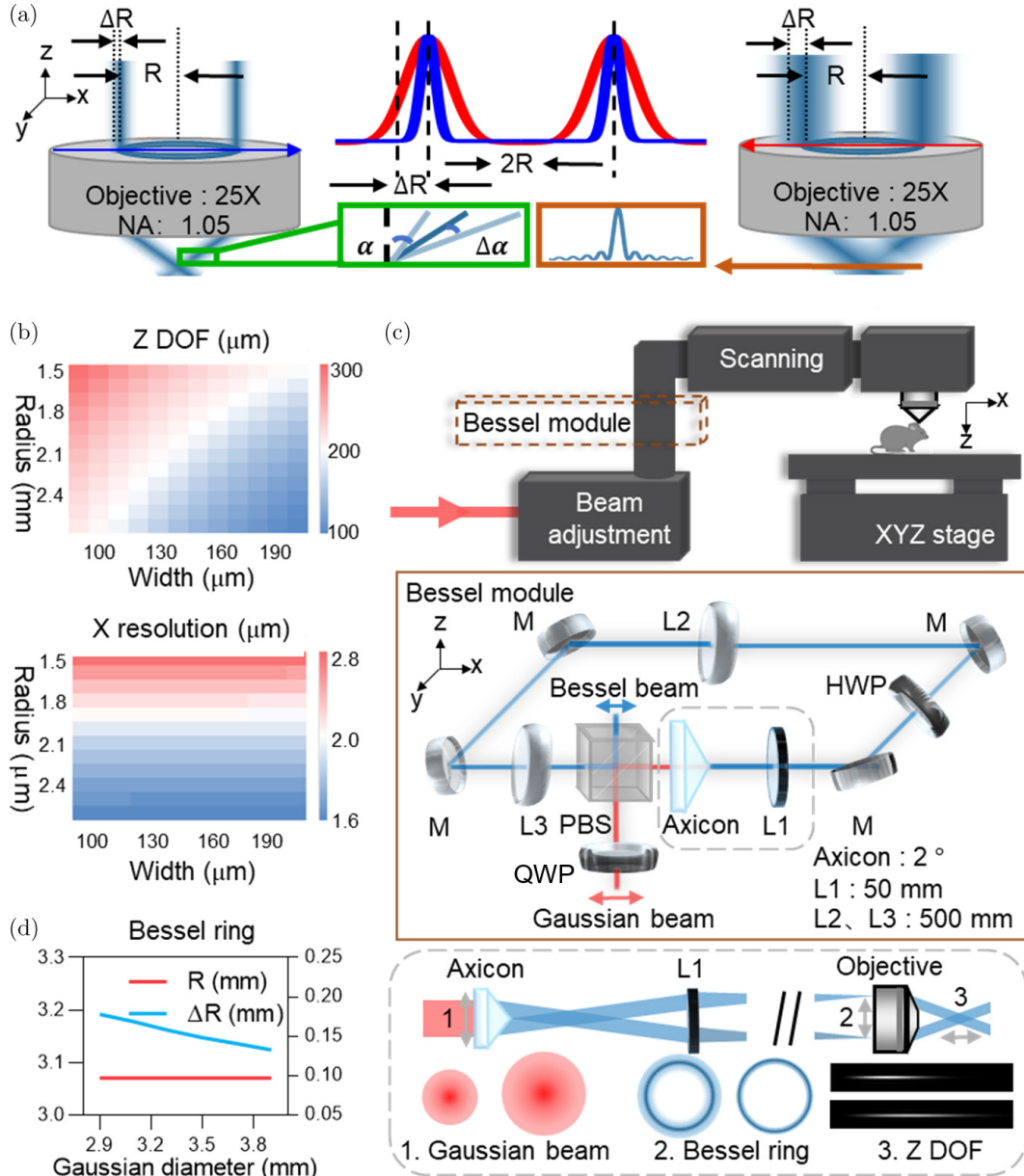


Fig. 1. Tunable-ring simulation and the optical module. (a) A schematic diagram of annular imaging. Gaussian distribution rings with the same diameter and different widths incident into the objective lens, forming different deflection angles. The intensity at the focal point is a Bessel distribution. (b) Simulation diagram of the correlation between the radius and width and the DOF along Z and lateral resolution. (c) Light path design based on the classical axicon with different Gaussian beam diameters for the generation of Bessel rings. (d) Simulation diagram of the correlation between the incident Gaussian diameter and ring radius and ring width in optical module.

independently adjust the annular width at the objective back focal plane while keeping the position of the center radius unchanged (Fig. 1(d)). That means, different incident diameters can independently adjust the focus depth while maintaining lateral resolution. In this process, the axicon converts the expansion of the Gaussian beam in the X and Y directions into the axial extension of the

Bessel beam, which is relayed to the focusing position through the conjugation of L1 and the objective lens without changing laterally.

Furthermore, we measured the axial and lateral intensity distribution of fluorescent 200 nm beads throughout the length of the Gaussian beam and the Bessel beam at different incident diameters. Conveniently, commercial 2PM provides several

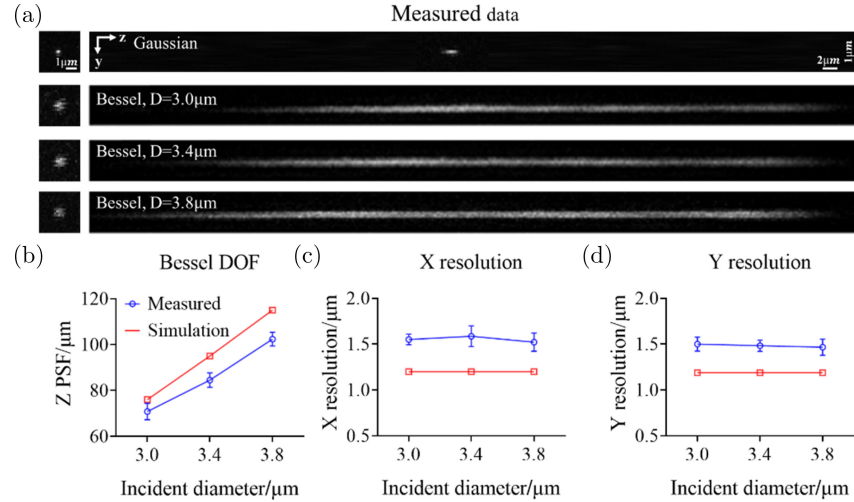


Fig. 2. The optical characterization. (a) Point spread function of Gaussian beam and Bessel beam in the experiment. For the Bessel beam, incident diameters of 3.0, 3.4 and 3.8 mm represent different DOF along Z, respectively. Comparison of experimental and simulation results of Bessel beam in (b) DOF along Z, (c) resolution along X, and (d) resolution along Y. Data were collected from four 0.2 μm diameter beads. Error bars, ±SEM.

diameter gradients, or, if not, add a telescope before the Bessel module. Figure 2 shows three representative DOF of 72.4, 84.6 and 101.2 μm at incident diameters of beam = 3, 3.4 and 3.8 mm, respectively. When the DOF is increased, their lateral resolution remained around 1.6 μm. These experimental values are in good agreement with simulation predictions, which represent that the increase in DOF does not compromise lateral resolution by adjusting the incident diameter.

In addition, we compared the imaging properties of the Gaussian beam and Bessel beam under the same incident diameter = 3.8 mm. The results showed that the imaging PSF of Gaussian illumination was 2.0 μm, while Bessel illumination was about 50 times greater. However, the lateral resolution of the Gaussian beam (0.8 μm) was better than that of the Bessel beam (1.6 μm). These properties between the Gaussian beam and the Bessel beam agree well with previous research.¹¹

3.3. In vivo imaging with adjustable Bessel system

To examine the performance of tunable volumetric imaging in nonhomogeneous media, we applied this design in imaging the GFP-labeled neurons of the primary visual cortex (V1 region) in awake mice, with a volume of 512 μm × 512 μm × 100 μm. At first, we continuously collected 50 two-dimensional images with 2 μm steps in Gaussian mode as a

contrast. Figures 3(a) and 3(b) show the volumetric neuronal structure at different depths with colored bands. Then, we acquired a single image at the same starting position with Bessel beams. As the incident diameter increased in a gradient, the longer DOF was translated into the ability to image more deep neurons gradually in a Bessel scan (Figs. 3(c)–3(e)). The longest DOF showed 75 neurons and the shortest DOF revealed 49 neurons (Fig. 3(f)). We also extracted the intensity contour of a neuron along the X and Y directions (Figs. 3(g) and 3(h)). In agreement with the theoretical predictions and the experimental results with fluorescent beads, the results indicated the remained spatial resolution for different diameters of Bessel beams. One notable fact is that for the same neuron, the result of the Gaussian beam and Bessel beam appears to be little difference in cell profile, compared to the resolution difference tested by beads in Fig. 2. Instead, the background noise difference is noticeable for different beams.

Given the volumetric property of the Bessel beam and the temporal resolution at 2PM, we investigated the dynamic calcium imaging of GCAMP6s-labeled neurons of the V1 region in mice. The visual stimuli with gratings moving in four directions was used to evoke calcium responses. Figure 4(a) shows the projective neuronal distribution under a Gaussian scan, and the calcium responses of only six neurons were recorded in a single scan (Fig. 4(b)). When imaging at the same frame rate (30 Hz), Bessel beams with longer DOF

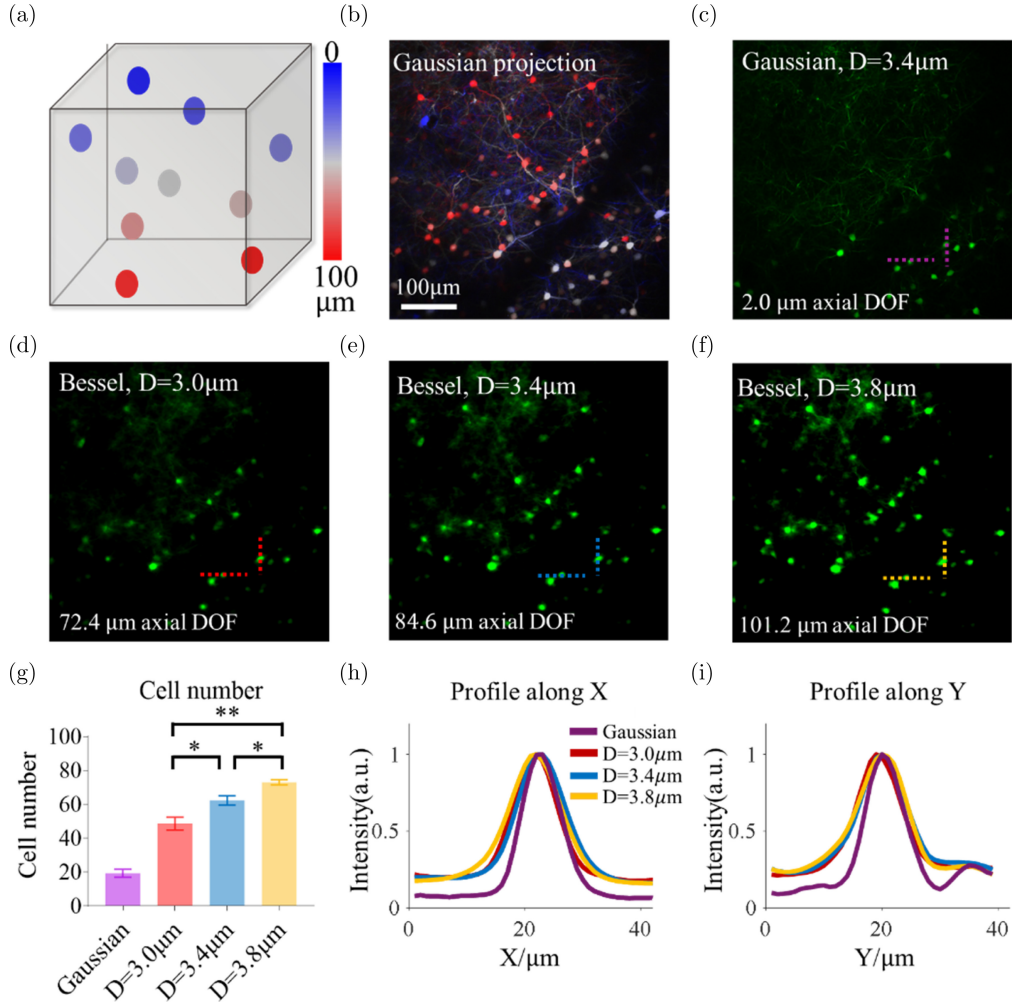


Fig. 3. Bessel imaging with different DOF to observe varying volumes of GFP-labeled neurons in a living mouse. (a) Different colors represent the depth distribution of neurons. (b) Average intensity projection (absolute depth 52–152 μm) of 0–100 μm Gaussian beam layer by layer, color-coded by relative depth. (c) Single-layer scanning image using Gaussian beam at the depth of 77 μm. (d)–(f) Volume images of Bessel focus at different diameters. Longer focal depth shows more and deeper neurons. The cell number (g) of varying Bessel DOF are counted and the same neuron is underlined along X and Y to display constant resolution (h) and (i). Error bars, \pm SEM. Kruskal–Wallis test with Dunn's *post hoc* test. $**p < 0.01$ and $*p < 0.05$.

revealed calcium activity from more neurons (Figs. 4(c)–4(e)). For cells# 1–5, similar responses were observed in three Bessel beams. For cells# 6–10, longer Bessel DOF could detect additional neurons (Figs. 4(f)–4(h)). These data highlight the performance of temporal resolution and the tunable ability of the Bessel module in volumetric imaging *in vivo*. In addition, we compared calcium peak intensity and orientation selectivity index (OSI) and found no significant difference.

4. Discussion

We chose the vector diffraction theory to analyze the variation law of DOF and lateral resolution

because it can be applied for high-NA objective and linear polarization systems, which is usually equipped in commercial 2PM. Although the conclusion is consistent with the previous studies on scalar diffraction, this derivation refines the correlation between the annular illumination of the Bessel beam and the point spread function and fills the gap in theory under practical application conditions. Since the simulation result shows that we can adjust the focal depth and keep the lateral resolution unaffected by changing the diameter of incidence in the system, theoretically, microresolution and a larger-volume image can be obtained with a larger beam diameter. Under the aperture limitations of the lens, the numerical simulation results show that the focal

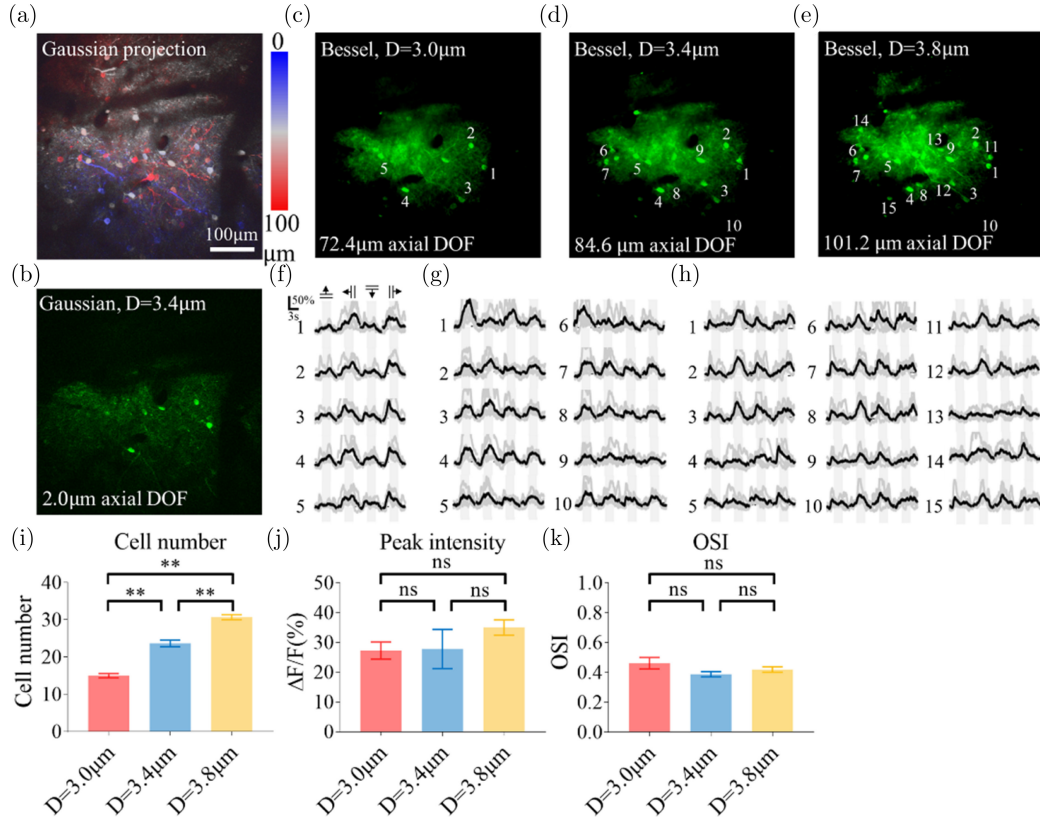


Fig. 4. Functional calcium imaging of GCaMP6s-labeled neurons in living mice using different Bessel DOF. (a) Mean intensity projection of 0–100 μm acquired by Gaussian stacks. (b) Image acquired by single Gaussian beam with 2.03 μm axial FWHM. (c)–(e) show images obtained by Bessel beam with diameters of 3.0, 3.4 and 3.8 mm. The corresponding longer DOF allows more volume neurons to be imaged. (f)–(h) were averaged calcium transient of neurons imaged by (c)–(e), respectively. Error bars, $\pm\text{SEM}$. Kruskal–Wallis test with Dunn’s *post hoc* test. ** $p < 0.01$; ns, nonsignificant.

depth can be reached at 300 μm when the beam diameter is 12 mm. This is also limited by power, however, because reshaping the Gaussian beam into a Bessel beam is already lossy.

Importantly, this design of an extended tunable Bessel beam is compatible with existing 2PM systems. In 2017, Masanori Matsuzaki reported that reducing the diameter of the Gaussian beam allows the imaging depth to reach 1200 μm ,³² which has been incorporated into the commercial 2PM systems with the extended imaging depth capabilities such as Olympus or Leica system. The diameter adjustment components coupled with our design allow flexible adjustment of the focal depth without replacing or rearranging any optics, which is friendly to those operating in biological experiments. Moreover, the module is flexible enough that an axicon with angle 1° or 0.5° and L1 lenses of other focal lengths can also be used to construct Bessel beams. Besides, the module is relatively inexpensive, costing about \$4200–6000.

In future work, we will investigate the possibility of application in light sheet microscopy,^{33,34} since the extended tunable Bessel beam is directly linked to the range of field of view and image resolution.^{35,36} This would enhance the flexibility of the design between different microscopes. On the other hand, several promising studies achieve adjustable focal depth by means of two axicons or algorithms.^{37,38} Its biological application in commercial two-photon system can be further explored.

5. Conclusions

Here, we reported a simplified method that can be integrated into a commercial TPM to produce a Bessel beam with extended DOF. The theoretical derivation and MATLAB simulation results suggested that changing the incident diameter could independently adjust the DOF and lateral resolution under linear polarization and high-NA. Further, we imaged the beads imaging to verify this

tuning method for sub-millimeter imaging DOF, and more importantly, established that the micron transverse resolution could be maintained in a classical system based on axicons. Then, we demonstrated the suitability of the system for biological imaging in awake mice by static and dynamic neuronal results.

Acknowledgments

We acknowledge helpful discussions with Wenzhi Sun and Jianglai Wu of Chinese Institute for Brain Research. We thank the MOST group members of Britton Chance Center for Biomedical Photonics for assistance with experiments and comments on the manuscript. We also thank the Optical Bioimaging Core Facility of WNLO-HUST for imaging systems.

This work was supported by STI2030-Major Projects (2021ZD0201001 to H. G.), the National Natural Science Foundation of China (61890951 and 31871027 to W. Z.) and Fundamental Research Funds for the Central Universities (HUST: 2019KFYXMBZ011, 2019KFYXMBZ039, 2018KFYXMP018, 2019KFYXMBZ009 to H.G.), CAMS Innovation Fund for Medical Sciences (CIFMS, 2019-I2M-5-014 to H.G.) and the director fund of the WNLO. Ting Mo and Yiran Liu contributed equally to this work.

Conflicts of Interest

The authors have no conflicts of interest relevant to this article.

References

1. F. Helmchen, W. Denk, “Deep tissue two-photon microscopy,” *Nat. Meth.* **2**(12), 932–940 (2005).
2. H. Li, J. Yu, R. Zhang, X. Li, W. Zheng, “Two-photon excitation fluorescence lifetime imaging microscopy: A promising diagnostic tool for digestive tract tumors,” *J. Innov. Opt. Health Sci.* **12**(5), 1–16 (2019).
3. B. Zhang, W. Gong, C. Wu, L. Hu, X. Zhu, K. Si, “Multidither coherent optical adaptive technique for deep tissue two-photon microscopy,” *J. Innov. Opt. Health Sci.* **12**(4), 1–11 (2019).
4. K. Wang, S. Tang, S. Wang, F. Lin, G. Zou, J. Qu, L. Liu, “Monitoring microenvironment of Hep G2 cell apoptosis using two-photon fluorescence lifetime imaging microscopy,” *J. Innov. Opt. Health Sci.* **15**(3), 1–9 (2022).
5. K. Svoboda, R. Yasuda, “Principles of two-photon excitation microscopy and its applications to neuroscience,” *Neuron* **50**(6), 823–839 (2006).
6. J. N. D. Kerr, W. Denk, “Imaging *in vivo*: Watching the brain in action,” *Nat. Rev. Neurosci.* **9**(3), 195–205 (2008).
7. W. R. Zipfel, R. M. Williams, W. W. Webb, “Nonlinear magic: multiphoton microscopy in the biosciences,” *Nat. Biotechnol.* **21**(11), 1369–1377 (2003).
8. W. Göbel, B. M. Kampa, F. Helmchen, “Imaging cellular network dynamics in three dimensions using fast 3D laser scanning,” *Nat. Meth.* **4**(1), 73–79 (2007).
9. T.-W. Chen, T. J. Wardill, Y. Sun, S. R. Pulver, S. L. Renninger, A. Baohan, E. R. Schreiter, R. A. Kerr, M. B. Orger, V. Jayaraman, L. L. Looger, K. Svoboda, D. S. Kim, “Ultrasensitive fluorescent proteins for imaging neuronal activity,” *Nature* **499**(7458), 295–300 (2013).
10. S. H. Huang, N. Irawati, Y. F. Chien, J. Y. Lin, Y. H. Tsai, P. Y. Wang, L. A. Chu, M. L. Li, A. S. Chiang, K. K. Tsia, S. W. Chu, “Optical volumetric brain imaging: Speed, depth, and resolution enhancement,” *J. Phys. D. Appl. Phys.* **54**(32), 323002 (2021).
11. F. O. Fahrbach, P. Simon, A. Rohrbach, “Microscopy with self-reconstructing beams,” *Nat. Photon.* **4**(11), 780–785 (2010).
12. G. Thériault, Y. De Koninck, N. McCarthy, Extended depth of field microscopy for rapid volumetric two-photon imaging, *Opt. Exp.* **21**(8), 10095 (2013).
13. G. Thériault, M. Cottet, A. Castonguay, N. McCarthy, Y. De Koninck, “Extended two-photon microscopy in live samples with Bessel beams: Steadier focus, faster volume scans, and simpler stereoscopic imaging,” *Front. Cell. Neurosci.* **8**, 1–11 (2014).
14. X. Wang, L. Wang, P. Lin, H. Xie, X. Xue, Q. Zeng, Y. Zhan, X. Chen, “Simulation of stimulated Raman scattering signal generation in scattering tissues excited by Bessel beams,” *J. Innov. Opt. Health. Sci.* **14**(3), 1–9 (2021).
15. T. A. Planchon, L. Gao, D. E. Milkie, M. W. Davidson, J. A. Galbraith, C. G. Galbraith, E. Betzig, “Rapid three-dimensional isotropic imaging of living cells using Bessel beam plane illumination,” *Nat. Meth.* **8**(5), 417–423 (2011).
16. D. Kleinfeld, G. Meng, Y. Liang, S. Sarsfield, W.-C. Jiang, R. Lu, J. T. Dudman, Y. Aponte, N. Ji, High-throughput synapse-resolving two-photon fluorescence microendoscopy for deep-brain volumetric imaging *in vivo*, *Elife* **8**(e40805), 1–22 (2019).
17. C. Liu, Z. Zhao, C. Jin, Y. Xiao, G. Gao, H. Xie, Q. Dai, H. Yin, L. Kong, “High-speed, multi-modal,

- label-free imaging of pathological slices with a Bessel beam," *Biomed. Opt. Exp.* **11**(5), 2694 (2020).
18. J. L. Fan, J. A. Rivera, W. Sun, J. Peterson, H. Haeberle, S. Rubin, N. Ji, "High-speed volumetric two-photon fluorescence imaging of neurovascular dynamics," *Nat. Commun.* **11**(1), 1–12 (2020).
 19. R. Lu, Y. Liang, G. Meng, P. Zhou, K. Svoboda, L. Paninski, N. Ji, "Rapid mesoscale volumetric imaging of neural activity with synaptic resolution," *Nat. Meth.* **17**(3), 291–294 (2020).
 20. R. A. Leitgeb, M. Villiger, A. H. Bachmann, L. Steinmann, T. Lasser, "Extended focus depth for Fourier domain optical coherence microscopy," *Opt. Lett.* **31**(16), 2450 (2006).
 21. S. Takanezawa, T. Saitou, T. Imamura, "Wide field light-sheet microscopy with lens-axicon controlled two-photon Bessel beam illumination," *Nat. Commun.* **12**(1), 2979 (2021).
 22. E. Wolf, Electromagnetic diffraction in optical systems, I. "Structure of the image field in an aplanatic system," *Proc. R. Soc. London. Ser. A. Math. Phys. Sci.* **253**(1274), 358–379 (1959).
 23. N. Ji, "Video-rate volumetric functional imaging of the brain at synaptic resolution," *Nat. Neurosci.* **20**, 620–628 (2017).
 24. J. H. McLeod, "The Axicon: A new type of optical element," *J. Opt. Soc. Am.* **44**(8), 592 (1954).
 25. P. Dufour, M. Piché, Y. De Koninck, N. McCarthy, "Two-photon microscopy with high depth of field using an axicon," *Appl Opt* **45**(36), 9246–52 (2006).
 26. O. Brzobohatý, T. Cižmár, P. Zemánek, "High quality quasi-Bessel beam generated by round-tip axicon," *Opt. Exp.* **16**(17), 12688 (2008).
 27. Y. Yang, B. Yao, M. Lei, D. Dan, R. Li, M. Van Horn, X. Chen, Y. Li, T. Ye, "Two-photon laser scanning stereomicroscopy for fast volumetric imaging," *PLoS One* **11**(12), 1–14 (2016).
 28. A. Song, A. S. Charles, S. A. Koay, J. L. Gauthier, S. Y. Thibierge, J. W. Pillow, D. W. Tank, "Volumetric two-photon imaging of neurons using stereoscopy (vtwins)," *Nat. Meth.* **14**(4), 420–426 (2017).
 29. R. Lu, M. Tanimoto, M. Koyama, N. Ji, "50 Hz volumetric functional imaging with continuously adjustable depth of focus," *Biomed. Opt. Exp.* **9**(4), 1964 (2018).
 30. H. Dehez, A. April, M. Piché, "Needles of longitudinally polarized light: Guidelines for minimum spot size and tunable axial extent," *Opt. Exp.* **20**(14), 14891 (2012).
 31. B. Richards, E. Wolf, "Electromagnetic diffraction in optical systems, II. Structure of the image field in an aplanatic system," *Proc. R. Soc. London.* **253** (1274), 358–379 (1959).
 32. M. Kondo, K. Kobayashi, M. Ohkura, J. Nakai, M. Matsuzaki, "Two-photon calcium imaging of the medial prefrontal cortex and hippocampus without cortical invasion," *Elife* **6**, 1–20 (2017).
 33. B. Gao, L. Gao, F. Wang, "Single-cell volumetric imaging with light field microscopy: Advances in systems and algorithms," *J. Innov. Opt. Health Sci.* **16**(2), 2230008 (2023).
 34. M. Wang, L. Wang, X. Zheng, J. Zhou, J. Chen, Y. Zeng, J. Qu, Y. Shao, B. Z. Gao, "Nonlinear scanning structured illumination microscopy based on nonsinusoidal modulation," *J. Innov. Opt. Health Sci.* **14**(5), 2142002 (2021).
 35. O. E. Olarte, J. Andilla, D. Artigas, P. Loza-Alvarez, "Decoupled illumination detection in light sheet microscopy for fast volumetric imaging," *Optica* **2**(8), 702 (2015).
 36. P. Y. Lin, S. P. L. Hwang, C. H. Lee, B. C. Chen, "Two-photon scanned light sheet fluorescence microscopy with axicon imaging for fast volumetric imaging," *J. Biomed. Opt.* **26**(11), 1–10 (2021).
 37. T. Breen, N. Basque-Giroux, U. Fuchs, I. Golub, "Tuning the resolution and depth of field of a lens using an adjustable ring beam illumination," *Appl. Opt.* **59**(15), 4744–4749 (2020).
 38. W. Yin, Y. Yang, R. Yang, B. Yao, "Tunable depth of focus with modified complex amplitude modulation of an optical field," *Appl. Opt.* **61**(12), 3502–3509 (2022).